

RESEARCH ARTICLE

10.1002/2016JF003819

Key Points:

- A 46 km transect of boreholes in Greenland shows seasonal phases of basal water pressure but similar median pressure in summer and winter
- Water pressure away from the ice margin is confined to the range of 0.8 to 1.1 of ice overburden pressure
- Hydraulic potential gradients are strongly influenced by the subglacial drainage system and cannot be derived solely from ice geometry

Supporting Information:

- Supporting Information S1

Correspondence to:

P. J. Wright,
patrickjwright@gmail.com

Citation:

Wright, P. J., J. T. Harper, N. F. Humphrey, and T. W. Meierbachtol (2016), Measured basal water pressure variability of the western Greenland Ice Sheet: Implications for hydraulic potential, *J. Geophys. Res. Earth Surf.*, 121, 1134–1147, doi:10.1002/2016JF003819.

Received 11 JAN 2016

Accepted 19 MAY 2016

Accepted article online 23 MAY 2016

Published online 11 JUN 2016

Measured basal water pressure variability of the western Greenland Ice Sheet: Implications for hydraulic potential

Patrick J. Wright¹, Joel T. Harper¹, Neil F. Humphrey², and Toby W. Meierbachtol¹

¹Department of Geosciences, University of Montana, Missoula, Montana, USA, ²Department of Geology and Geophysics, University of Wyoming, Laramie, Wyoming, USA

Abstract The gradient of the hydraulic potential field at the ice-bedrock interface beneath the Greenland Ice Sheet (GrIS) dictates the routing and energetics of subglacial water, thereby influencing drainage system characteristics and sliding dynamics. In the ablation zone of the GrIS, variable water pressure due to an active subglacial drainage system and basal topography with high relief potentially interact to drive unknown spatial patterns and temporal changes in the hydraulic potential field. Here we present a suite of water pressure measurements collected in 13 boreholes along a 46 km transect on the western GrIS to investigate the role of spatial and temporal basal water pressure adjustments in hydraulic potential gradient dynamics. All borehole sites show pressures with similar seasonality, having relatively steady and high values during winter, variable and irregular behavior during spring and fall, and diurnal cycles that can persist for multiple weeks during the peak melt season. Despite much higher variability during the melt season, the median pressure of the summer period is nearly the same as the median pressure of the winter period. However, time variability of water pressure due to basal drainage processes can force changes in the magnitude and orientation of the hydraulic potential field over diurnal periods. We find that the basal water pressure across the transect generally mimics the ice thickness field but with superimposed large pressure gradients that develop at shorter scales within the basal drainage system. This leads to a complex hydraulic potential field across regions of similar ice thickness.

1. Introduction

The subglacial drainage system imparts a key control on the sliding speed of the Greenland Ice Sheet (GrIS) by dictating the variability of basal water pressure and areas of coupling between the ice sheet and its bed. The drainage system evolves seasonally [e.g., *Hoffman et al.*, 2011] in response to input of surface melt, which rapidly reaches the bed via moulins and crevasses [*Das et al.*, 2008; *Catania and Neumann*, 2010; *McGrath et al.*, 2011]. Active subglacial drainage systems likely evolve inward from the margin [e.g., *Chandler et al.*, 2013], establishing networks of channelized and distributed drainage elements which define drainage basin areas. The routing of water in these networks is set by the direction and magnitude of the hydraulic potential gradient. In order to determine potential gradients, and hence the broad constraints on basal water flow, the bed topography and basal water pressure field must be well known (see section 2).

Several reviews of subglacial hydrology in alpine glacier settings [e.g., *Hooke*, 1989; *Hubbard and Nienow*, 1997; *Fountain and Walder*, 1998] have evaluated seasonal evolution of borehole water pressure records and provided interpretations for water routing and glacier sliding. Although a wide body of previous work has established important foundations for understanding subglacial water flow, prior alpine glacier findings have uncertain application to large ice sheets where thick ice can induce rapid creep closure, water flows at the bed over many tens of kilometers, and critically, relatively shallow surface slopes (e.g., often 1° or less) drive water flow, sometimes over high-relief bed topography. Early borehole measurements in GrIS revealed basal water pressure near overburden, but records typically spanned only a few days [*Thomsen and Oleson*, 1990, 1991; *Thomsen et al.*, 1991; *Iken et al.*, 1993]. Only recently have measurements become more temporally and spatially extensive and have demonstrated that water pressure undergoes diurnal cycles and seasonal variability [*Lüthi et al.*, 2002; *Meierbachtol et al.*, 2013; *Andrews et al.*, 2014; *van de Wal et al.*, 2015].

Recent development of bed digital elevation models (DEMs) using radar and mass conservation techniques have revealed basal topography beneath the GrIS with much greater relief than previously assumed [*Bamber et al.*, 2013; *Lindbäck et al.*, 2014; *Morlighem et al.*, 2014]. In particular, the ablation zone of the

western GrIS is characterized by reaches with steep-walled bedrock troughs. The ice surface remains relatively smooth in these regions, with shallow surface slopes and only muted expressions of bedrock topography, resulting in highly variable ice thickness. Despite the increasing fidelity of topographic data, however, a lack of constraints on basal water pressure continues to invoke large uncertainty in hydraulic potential gradients.

In this study we use measurements collected in 13 boreholes to assess temporal and spatial scales of basal water pressure variability along a 46 km transect in western Greenland. Borehole records collected during 2010–2015 span summer and winter periods and include six sites ranging from near-margin to inland conditions. As such, the records permit assessment of spatial pressure gradients at the site to regional scale as well as temporal changes over daily and seasonal periods. We use these results to examine the sensitivity of the potential gradient field to variability in water pressure.

2. Gradients of Water Pressure and Hydraulic Potential

Hydraulic potential is composed of an elevation potential and a pressure potential

$$\phi_h = \rho_w g z_b + P_w, \quad (1)$$

where P_w is water pressure, z_b is the bed elevation, ρ_w is density of water, and g is the acceleration due to gravity. Multiplying P_w in equation (1) by (P_i/P_i) allows the pressure term to be equivalently expressed as a fraction of the ice overburden pressure

$$\phi_h = \rho_w g z_b + \rho_i g H \frac{P_w}{P_i}, \quad (2)$$

where H is ice thickness ($z_s - z_b$), P_i is ice overburden pressure, and ρ_i is ice density. The hydraulic potential gradient is then defined by the negative gradient of ϕ_h

$$-\nabla \phi_h = -\rho_w g \nabla z_b - \rho_i g \nabla H \frac{P_w}{P_i} - \rho_i g H \nabla \left[\frac{P_w}{P_i} \right]. \quad (3)$$

The third term on the right side of the expression is nearly always neglected by invoking the assumption that basal water pressure gradients are solely a function of the ice overburden. The basal water pressure is then either set equal to the ice pressure or sometimes allowed to deviate as a spatially invariant fraction of overburden pressure. Equation (3) is then commonly approximated [e.g., *Shreve, 1972; Cuffey and Paterson, 2010*] by

$$-\nabla \phi_h = -\rho_i g \left[\frac{P_w}{P_i} \nabla z_s + \left[\frac{\rho_w}{\rho_i} - \frac{P_w}{P_i} \right] \nabla z_b \right]. \quad (4)$$

The above expression relates basal water pressure gradients directly to changes in ice thickness, as derived from surface and bed topography via ∇z_s and ∇z_b . In other words, equation (4) represents situations where the water pressure field mimics the ice thickness field or some spatially invariant fraction thereof. Equation (4) has been applied to Greenland at the basin scale [e.g., *Tedstone et al., 2014; Lindbäck et al., 2015*] and the ice sheet scale [*Lewis and Smith, 2009; Liston and Mernild, 2012; Livingstone et al., 2013*] to delineate drainage basins and associated sediment and water fluxes. Adjustment of water pressure has been found to strongly impact the computed potential gradients [*Lindbäck et al., 2015*].

In situations where bed slopes are steep and pressures are high, the critical role of water pressure in determining potential gradients is illustrated by a comparison of the ratio of the surface gradient multiplier [P_w/P_i] to the bed gradient multiplier [$(\rho_w/\rho_i) - (P_w/P_i)$] under varying water pressure (Figure 1). The relationship is highly nonlinear such that small changes in water pressure at values near overburden result in large changes in the hydraulic potential gradient if the disparity between surface and bed slopes is substantial. As shown later, these conditions are common in western Greenland.

A second complication to hydraulic potential gradients of western Greenland stems from the basal drainage system, which may develop strong water pressure gradients that are unrelated to ice thickness: i.e., the third term in equation (3) may be large. Strong pressure gradients in the subglacial drainage system are often

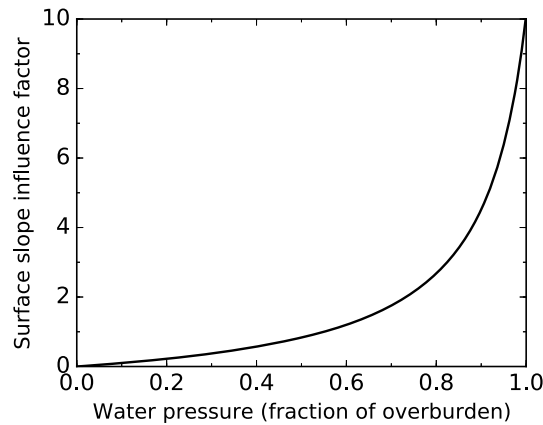


Figure 1. Influence of ice surface slope on the total hydraulic potential gradient as a function of basal water pressure. “Surface slope influence factor” of 1 indicates that surface slope and bed slope contribute equally to the total potential gradient. A factor of 10 indicates that the surface is 10 times more influential than the bed.

induced by basal processes such as water flux imbalances, melt-back of ice walls, creep closure of the ice roof, and cavity opening from sliding. Pressure gradients have been observed by direct measurement [e.g., Meierbachtol *et al.*, 2013; Andrews *et al.*, 2014] implying active basal processes in Greenland and have also been inferred from physics-based modeling of drainage system evolution [e.g., Hewitt *et al.*, 2012; Hewitt, 2013; Werder *et al.*, 2013]. Modeling work has also suggested that water pressure gradients can be induced from spatially variable normal stress in the ice resulting from stress transfer between slippery and sticky patches at the bed [Ryser *et al.*, 2014a, 2014b]. Furthermore,

these spatial water pressure gradients are subject to the additional complication that water pressure may vary in time due to seasonally and diurnally varying melt input.

The hydraulic potential gradient at the bed of GrIS is therefore expected to be strongly controlled by details of the water pressure field and its time and space gradients: $\nabla\phi_h$ should be sensitive to small changes in the magnitude of pressure because of steep bed slopes, and $\nabla\phi_h$ may also be sensitive to non-overburden-related pressure gradients which arise from basal processes and seasonal development of a basal drainage system. Our working knowledge of these details, however, is quite limited owing to few observations of subglacial water pressure.

3. Methods

Boreholes were drilled using hot water methods at six locations along a transect moving inland from Isunnguata Sermia, on the southwest margin of the GrIS (Figure 2). For the borehole locations described below, all distances inland are reported as distance from the terminus of Isunnguata Sermia. Boreholes are named as [distance]-[two-digit year][letter], according to distance inland (km), two-digit year of drilling, and a letter identifier for multiple boreholes at each site.

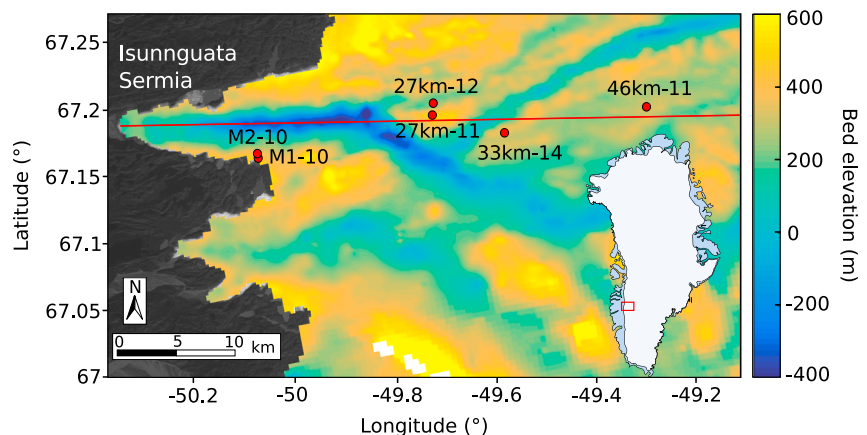


Figure 2. Locations of borehole sites along the study transect in western Greenland, shown with 250 m resolution bed topography [Lindbäck *et al.*, 2014]. Red line indicates the profile line in Figure 11.

Table 1. Location, Ice Depth, and Length of Record for All Boreholes

Borehole ^{a,b}	Latitude (deg)	Longitude (deg)	Ice Depth (m)	Length of Record (yyyy-mm-dd) (# Days)
M1-10	67.162	-50.063	99	2010-06-15 to 2010-09-20 (98)
M2-10A	67.167	-50.067	149	2010-06-22 to 2010-09-20 (91)
M2-10B	67.167	-50.066	146	2010-06-26 to 2010-09-11 (78)
27km-11A*	67.195	-49.720	458	2011-07-10 to 2012-07-10 (367)
27km-11B	67.195	-49.719	466	2011-07-10 to 2011-09-14 (67)
27km-11C	67.195	-49.719	460	2011-07-10 to 2011-09-14 (67)
27km-12A*	67.204	-49.718	696	2012-06-16 to 2013-07-23 (403)
27km-12B*	67.204	-49.718	688	2012-06-17 to 2013-07-16 (395)
27km-12C*	67.204	-49.718	696	2012-06-21 to 2013-07-16 (391)
33km-14A	67.182	-49.575	674	2014-07-17 to 2014-08-08 (23)
33km-14B*	67.182	-49.575	661	2014-07-27 to 2015-04-22 (270)
46km-11A	67.201	-49.289	821	2011-07-15 to 2011-09-14 (62)
46km-11B	67.201	-49.289	815	2011-07-20 to 2011-09-14 (57)

^aBorehole ID format is [distance]-[two-digit year][multiple borehole letter], where M1 and M2 are near-margin sites, distance (km) for remaining sites is distance from Issunguata Sermia terminus, and two-digit year indicates beginning of record for each borehole.

^bAsterisk indicates boreholes with overwinter records shown in Figures 3 and 8.

Three boreholes drilled in 2010 at two near-margin locations are identified separately (M1-10, M2-10A, and M2-10B). These sites are approximately 12 km from the terminus of Issunguata Sermia; however, they are located very near the lateral margin at a point where Issunguata Sermia exits the main body of the ice sheet. Boreholes M2-10A and M2-10B are colocated within 10 m and are approximately 1 km from the lateral margin (ice depth ~150 m), and borehole M1-10 is located approximately 450 m from the lateral margin (ice depth ~100 m).

Sites 27km-11 and 27km-12 are located approximately 27 km inland (drilled in 2011 and 2012, respectively). Site 27km-11 overlies a ridge in bedrock topography (ice depth ~460 m) and is located approximately 1 km south of site 27km-12, which overlies a bedrock trough (ice depth ~700 m). Three boreholes at each site are colocated within 20–30 m. Site 33km-14 (ice depth ~670 m) has two boreholes colocated within 150 m and overlies a high plateau in bedrock topography with a major northeast-southwest trending bedrock trough north of the site. Site 46km-11 (ice depth ~820 m) has two boreholes colocated within 20 m and is located ~30 km below the long-term equilibrium line altitude (ELA) [van de Wal *et al.*, 2012]. Appropriate drilling speed determined by monitoring the drill stem's load on the drill tower ensures that boreholes are drilled vertically with a free-hanging lead drill stem [Humphrey and Echelmeyer, 1990], such that distances between colocated boreholes at the surface are equivalent to distances at the bed. Distance inland, latitude, longitude, ice depth, and length of record for each borehole are listed in Table 1.

Hole depth was confirmed with three independent measurements: depth marks on the drill hose, depth marks on instrumentation cable lowered down the borehole, and depth from a digital odometer on the drill. From these measurements, we estimate the accuracy of reported borehole depths to be <1.5% of total ice thickness (± 2 m for margin locations, ± 12 m for inland locations). Additional details of borehole drilling and instrumentation methods are described by Meierbachtol *et al.* [2013] (supporting information).

Boreholes were instrumented near the bed with pressure transducers logging at 5 or 15 min intervals during summer and 15 or 30 min intervals during winter. Pressure transducers were lowered to a position ~25–50 cm above the bed, with boreholes then freezing shut except near the bed where temperature measurements at each site show that the ice is temperate [Harrington *et al.*, 2015]. The length of pressure records is limited by the connection of the sensor cables, which can fail due to stretching or rupture from crevassing at near-margin locations.

Water pressure is most commonly reported in this study as a fraction of overburden (OB) pressure. For all calculations, we assume an ice density of 910 kg m^{-3} . However, ice density can vary due to air bubbles, liquid water, or debris and impurities and can commonly range between 880 and 917 kg m^{-3} [Cuffey and Paterson, 2010]. Uncertainty is analyzed for the combined maximum and minimum errors due to pressure transducer resolution (± 0.1 m), ice depth measurements, and ice density. Resulting uncertainty in scaled overburden

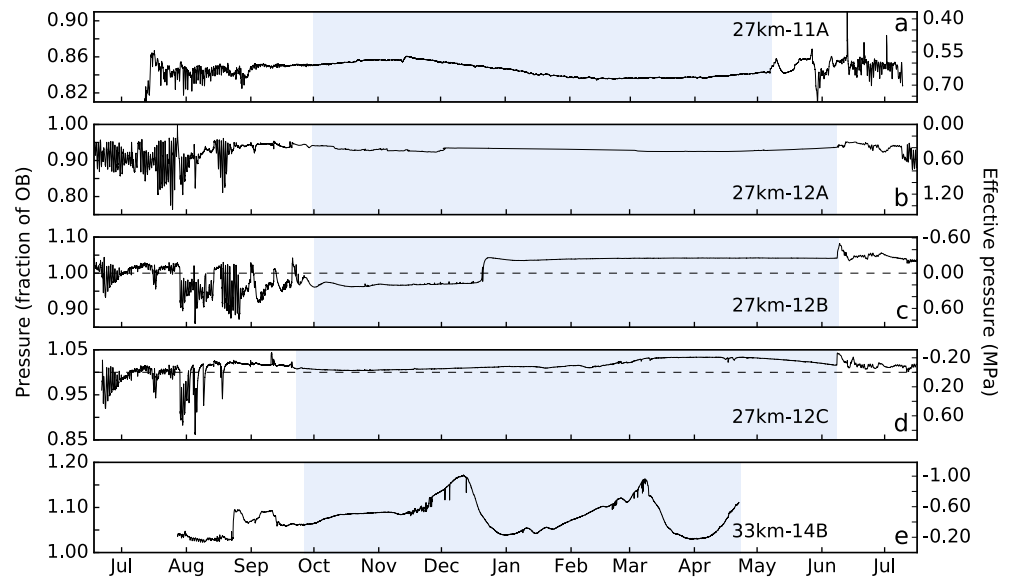


Figure 3. Annual water pressure records from boreholes (a) 27km-11A, (b) 27km-12A, (c) 27km-12B, (d) 27km-12C, and (e) 33km-14B. The characteristic winter period for each record is shaded in blue. Note that y axis scales differ between panels to highlight details of individual records.

calculations varies slightly as a function of ice depth, with a maximum range from all error sources for our deepest borehole of -0.022 OB to $+0.047$ OB. This uncertainty is predominantly a function of the possible range in values for ice density. If the range of ice density is constrained to $900\text{--}917\text{ kg m}^{-3}$, the maximum range in uncertainty is reduced to -0.022 OB to $+0.026$ OB.

4. Water Pressure Results

4.1. Seasonal Phases

Borehole water pressure throughout the transect shows characteristic seasonal phases, with a clear distinction between melt season and winter behavior (Figure 3). Winter water pressure is characterized by a confined range that dominates for nearly 8 months of the year. Pressure during winter commonly shows low-frequency variability over weeks and months, although in one case bimodal behavior is observed, with a sudden increase of nearly 0.07 OB (44 m head) over a 5 day period (borehole 27km-12B; Figure 3c). The winter record for borehole 33km-14B (Figure 3e) is an outlier in behavior from other winter records, showing two cycles with a range of 0.12 OB (75 m head) evolving over 2–3 month periods.

The melt season includes an initial spring phase, a period of regular diurnal cycles, and a fall “shutdown” phase. In the spring the winter-melt season transition is distinct, characterized by a sudden sharp increase in pressure usually occurring in early June. In two boreholes (27km-11A and 27km-12A) the spring activation event is $0.005\text{--}0.02$ OB in magnitude ($3\text{--}6$ m head), which is subsequently followed within days or weeks by further pressure increases. The spring event in two boreholes, 27km-12B and 27km-12C, consists of a single rapid increase of $0.03\text{--}0.04$ OB ($17\text{--}26$ m head). Spring events often record the maximum pressure values for an annual period; for example, the spring activation event in 2013 for borehole 27km-12B (Figure 3c) reaches a maximum pressure of 1.08 OB.

The period of summer diurnals weakens and becomes more irregular in late August or September, defining a transition to fall behavior. The fall phase is often characterized by an evolution to higher pressures and a dampening of diurnal variability over a period of weeks until a relatively constant pressure is reached and sustained into winter, indicating the melt season-winter transition.

4.2. Diurnal Cycles

All boreholes show periods of regular diurnal variability during midsummer (Figures 3 and 4). However, the magnitude and range of diurnal swings can be highly variable between boreholes and does not necessarily

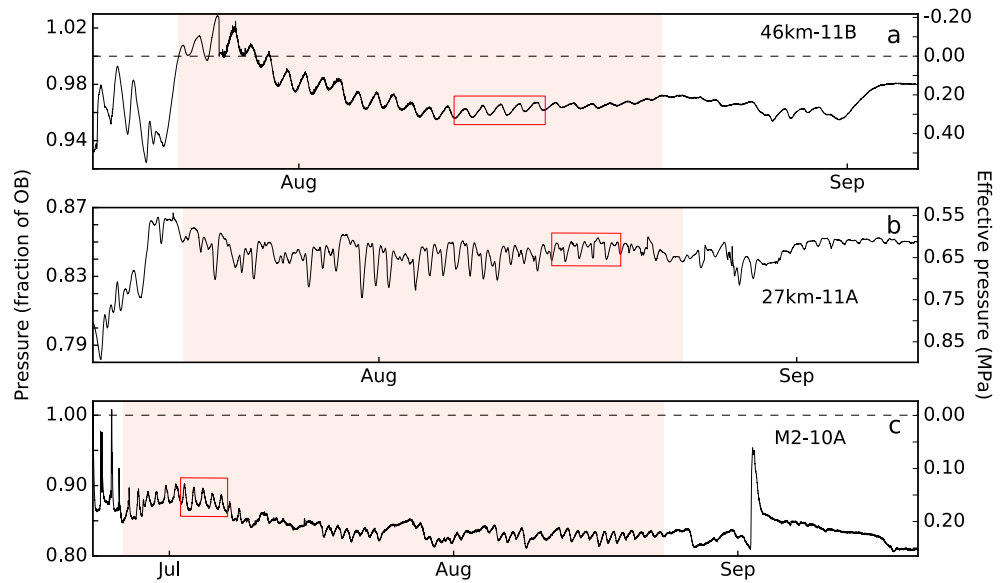


Figure 4. Melt season water pressure records for boreholes (a) 46km-11B, (b) 27km-11A, and (c) M2-10A. The period representing “summer diurnals” for each record is shaded in red. Five-day periods selected for diurnal analysis (Figure 5) are indicated with red boxes. Note that y axis scales differ between panels to highlight details of individual records.

follow a perfect sinusoid. For example, three distinct end-member types of diurnal cycles were observed: a symmetric mode where time is equally partitioned across the pressure range; a high-pressure dominated mode, where higher pressures occupied a greater fraction of the day; and a low-pressure dominated mode, where more of the day was occupied by lower pressure (Figure 5).

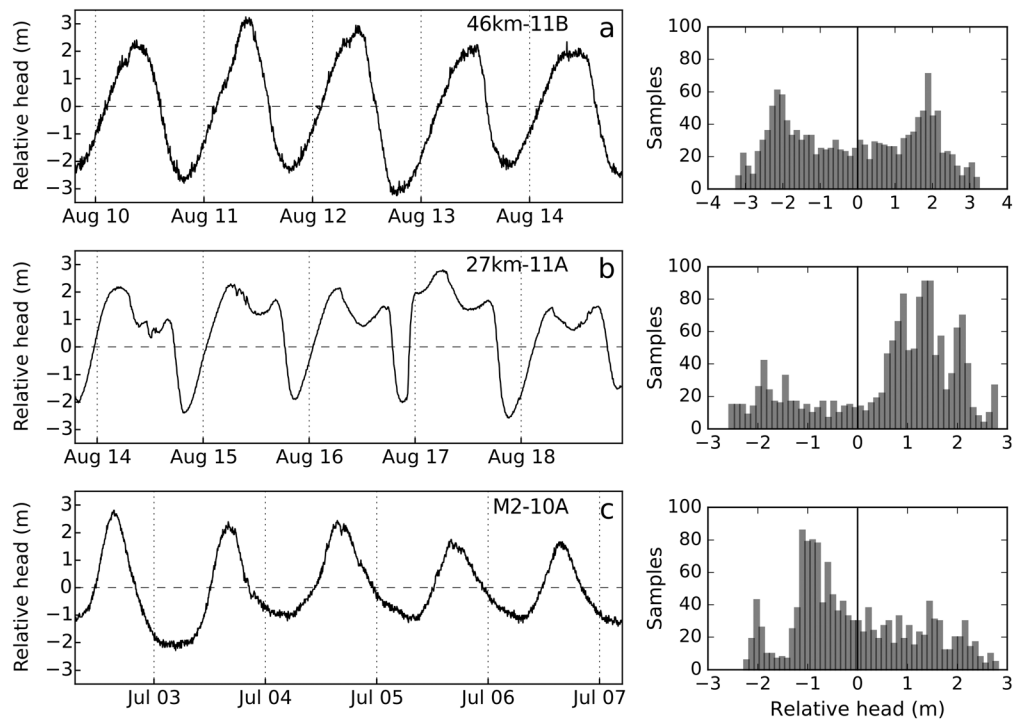


Figure 5. Three modes of diurnal water pressure variability, corresponding to 5 day periods indicated in Figure 4. (a) A symmetric mode from site 46km-11B. (b) A high-pressure dominated mode from site 27km-11A. (c) A low-pressure dominated mode from site M2-10A. Corresponding histograms show distribution of data.

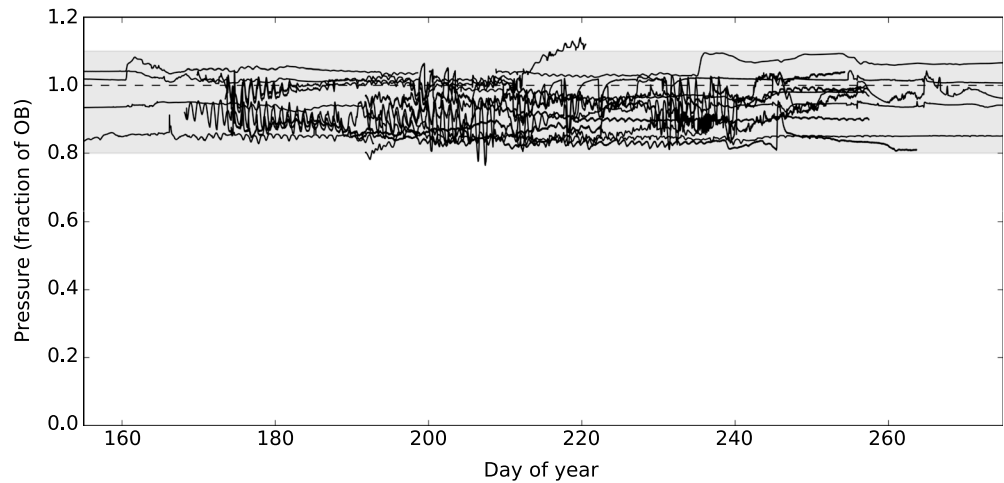


Figure 6. Melt season basal water pressure records from all 12 boreholes showing limited range of variability. Near-margin, shallow-ice borehole M1-10 is interpreted to be an outlier as described in the text and omitted here. All pressure records throughout the transect are confined to a range of approximately 0.8–1.1 of overburden pressure, as indicated by the shaded region.

Histograms based on 5 day detrended periods demonstrate the difference between the three cases in the time distribution of water pressure. In the symmetric mode (Figure 5a), water pressure resides at high and low magnitudes for approximately equal portions of the diurnal cycle (51% below, 49% above). In the high-pressure dominated mode (Figure 5b) water pressure is sustained above the median value for 73% of the period, and in the low-pressure dominated mode (Figure 5c) pressure remains below the median value for 58% of the period. There is no clear dominance of one type of behavior across the transect; however, the mode that is established for an individual borehole tends to stay consistent throughout the summer diurnal period (Figure 4).

Regardless of the shape of diurnal variability, 12 of the 13 boreholes show diurnal cycles that are predominantly confined to a distinct range of 0.8–1.1 OB (Figure 6). Once diurnal cycles are established, minimum pressures reached during July or August are typically the lowest pressures of the annual record for a borehole. A low pressure of 0.76 OB reached during late July in borehole 27km-12A (Figure 3b) defines the minimum pressure recorded in the 12-borehole suite. However, we see no evidence for consistent subseasonal decreasing trends in the magnitude of diurnal maximum or minimum pressures. Periods of diurnal cycles can show occasional multiday trends of slightly increasing or decreasing pressure, but each pressure record remains constrained within the range throughout the melt season (Figure 6).

Pressure data from borehole M1-10 are unique from the other 12 records. Located just 450 m from the lateral margin of Isunnguata Sermia with an ice depth of 99 m, water pressure records at this site show large diurnal pressure swings (68 m head), reaching a melt season minimum near 0.3 OB yet with daily maximum pressures remaining above overburden throughout the melt season. Despite low minimum pressures, the median pressure for the entire record remains high at 0.86 OB, largely due to diurnal maximums consistently near overburden throughout the melt season.

4.3. Spatial Gradients

Our measurements demonstrate that substantial gradients in water pressure can exist between adjacent boreholes spaced tens to hundreds of meters apart. Pressure differences arise from hole-specific temporal fluctuations occurring over time periods of hours to weeks. For example, boreholes 46km-11A and 46km-11B are colocated within 20 m and both boreholes show consistent diurnal cycles (Figure 7). However, the two pressure records are consistently offset throughout the melt season by ~ 0.06 of OB (~ 40 m head). This difference in head represents a water pressure gradient of $\sim 20 \text{ kPa m}^{-1}$. Because the ice thickness measured directly in the boreholes differs by only 6 m, these gradients can only be attributed to basal drainage system processes (the overburden pressure gradient is an order of magnitude less).

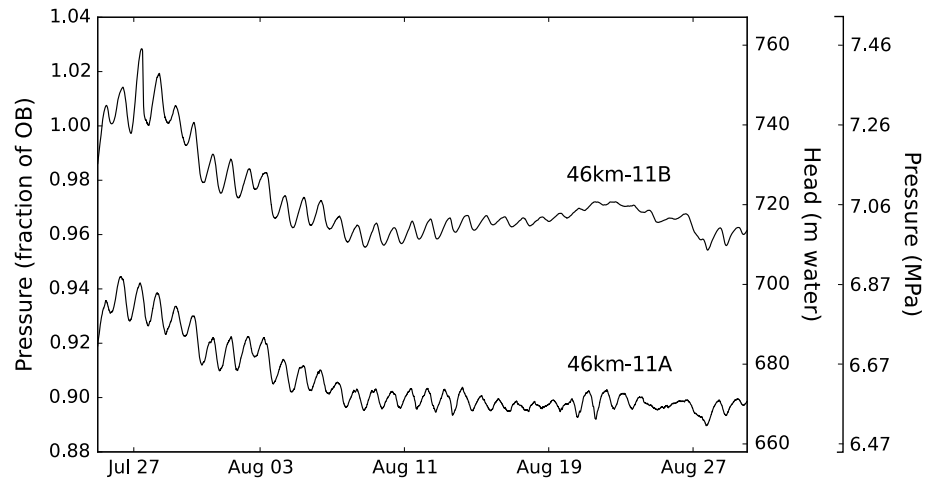


Figure 7. Pressure records during 2011 from boreholes 46km-11A (ice depth 821 m) and 46km-11B (ice depth 815 m). Boreholes are collocated at the site within 20 m.

Boreholes spaced tens to hundreds of meters apart can show pressure differences within the same range of values (~0.8 to >1.0 OB) as sites tens of kilometers apart, when expressed as a fraction of the overburden pressure (the exception is the near-margin hole, which we argue in section 5.1 is a special case). The pressure potential, however, shows very large changes across the study domain driven by overall changes in ice sheet thickness. Long length scales between sites yield potential gradients averaging 0.16 kPa m^{-1} as ice thins toward the margins. Despite the fact that large local drainage system-driven pressure gradients are not upheld over longer intersite length scales, very large changes in ice thickness, such as those existing along

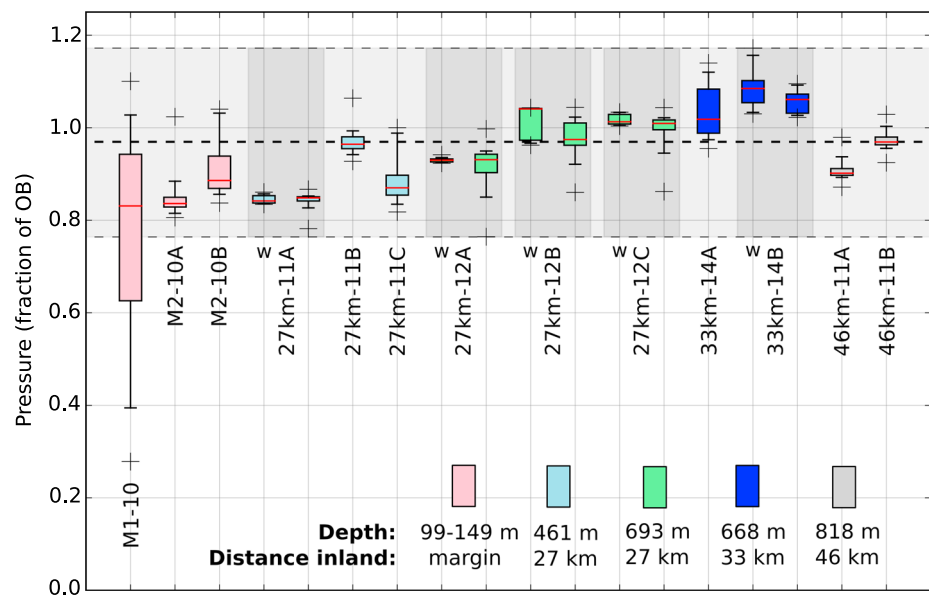


Figure 8. Box plots of basal water pressure data for all boreholes, where box color corresponds to distance from terminus (see Figure 2). For boreholes with overwinter records, corresponding winter and melt season periods are shown in shaded pairs, where winter records are indicated with “w.” For boreholes with only melt season records, all data in the record are represented. Box center lines are median, boxes span the first and third quartiles, whiskers extend to 5th and 95th percentiles, and crosses indicate maximum and minimum points. Thick dashed line is the weighted annual mean, and shaded region spans the minimum and maximum values of the 12-borehole suite (excepting hole M1-10).

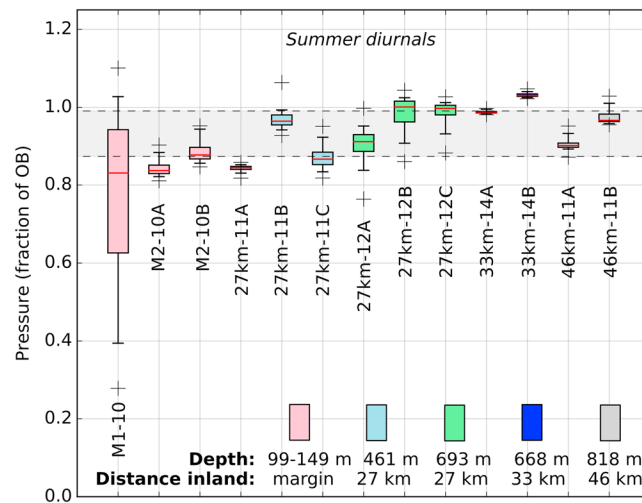


Figure 9. Box plots of water pressure data for the summer diurnal period, where box color corresponds to distance from terminus. Shaded region is the imposed diurnal range used for sensitivity testing of the hydraulic potential gradient (5th to 95th percentiles from borehole 27km-12B, centered at the data set mean median). Box center lines are medians, boxes span the first and third quartiles, whiskers extend to 5th and 95th percentiles, and crosses indicate maximum and minimum points.

walls of steep bedrock troughs, can generate pressure gradients over hundreds of meters that are nearly 20 times greater than the overall transect gradient.

4.4. Summary Statistics

Box plots summarizing all pressure records from each borehole demonstrate no consistent trends in scaled overburden pressure as a function of ice thickness or distance inland from the margin (Figure 8). In some cases, boreholes with thicker ice and greater distance inland clearly show higher pressures than more near-margin, shallower locations. For example, boreholes at sites 27km-12 and 33km-14 generally show pressures that are higher than at sites M2-10 and 27km-11. However, evidence for the opposite relationship is equally common. The melt season record of borehole M2-10B shows

consistently higher pressure than two of three boreholes at site 27km-11, with ice thickness that is 300 m less and a location 15 km nearer to the margin. In addition, both boreholes at the most inland site (46km-11) show pressures that are lower than all boreholes at site 33km-14 and lower than two of three records at site 27km-12. Similarly, no spatial trends are obvious during the period of diurnal pressure swings (Figure 9).

To assess seasonal evolution of water pressure from the winter to the melt season, we separate winter and melt season data for the five boreholes with annual records (indicated with shaded box plot pairs in Figure 8). For three of these boreholes there is essentially no change from winter to melt season median pressure (<0.01 OB), and in borehole 33km-14B the winter median pressure decreases by only 0.02 OB. This consistent seasonal behavior has exception only in borehole 27km-12B, showing a decrease from winter to melt season median pressure of 0.07 OB resulting from distinct bimodal winter behavior for this borehole which establishes a relatively high median for the winter record (Figure 3c).

The minimum and maximum values recorded in the 12-borehole suite are 0.76 OB and 1.17 OB, respectively (shaded region in Figure 8). The annual weighted mean pressure for the transect remains near overburden at 0.97 OB (Figure 8, thick dashed line). This calculation of the annual mean is supported by all data in the 12-borehole suite (data from borehole M1-10 are not included for reasons discussed in section 5.1), but this result may be biased by the weighting method (see supporting information), where the winter and melt season are each assigned a fixed period of the year which may be an inaccurate representation of the actual seasonal timing for a given site. For comparison, we also present a simple calculation of annual mean pressure using only the four boreholes with yearlong records. Averaging the median values of annual data resampled to 30 min intervals for the full record of these boreholes, the annual mean is only 0.01 OB lower at 0.96 OB. Either treatment of the data set therefore constrains the annual mean pressure between 0.96 and 0.97 OB.

5. Discussion

5.1. Representativeness of Borehole Pressures

The basal water pressure summary statistics presented here rely on borehole measurements that sample small areas of the bed at specific locations and are limited to the seasonal characteristics that may be unique to the years of measurement. This brings into question how representative these results are in both time and space. Several lines of evidence, however, suggest that our data are broadly representative of the study region.

Table 2. Summary Data for All Previous Borehole Water Pressure Measurements on the GrIS

Study	Pressure Range (Fraction of OB)	Number of Boreholes ^a	Distance Inland ^b (km)	Ice Depth (m)
This study, 12-borehole suite	0.76–1.17	13	0.5–46	146–821
<i>Van de Wal et al.</i> [2015]	0.93–1.00	2	15	not reported
<i>Andrews et al.</i> [2014]; <i>Ryser et al.</i> [2014a, 2014b]	0.90–1.13	6	20–30	620–700
<i>Lüthi et al.</i> [2002]	1.00–1.01	2	55	830
<i>Iken et al.</i> [1993]	0.96–1.00	2	50	1600
<i>Thomsen and Oleson</i> [1990, 1991]; <i>Thomsen et al.</i> [1991]	0.79–1.05	12	1–8	180–350

^aNumber of boreholes with published water pressure records.

^bDistance inland is from the terminus of Issunguata Sermia (this study, exception to near-margin holes) or from the terminus of Jakobshavn Isbræ terminus [*Iken et al.*, 1993; *Lüthi et al.*, 2002]. All other distances are approximate from the ice margin.

Borehole sites in our transect sampled multiple topographic regimes including a bedrock trough (27km-12), a bedrock ridge (27km-11), relatively flat bed areas away from troughs (33km-14 and 46km-11), and the wall of a major bedrock trough near the margin (M2-10) (Figure 2). The boreholes also sampled a wide range of ice depths and distances inland from the margin (Table 1). Across the range of locations sampled, borehole water pressure measurements throughout the transect show similar characteristic seasonal phases and variability within a confined range of values (Figures 3, 6, and 8). Further, no distinct trends in pressure as a function of distance inland or ice depth were identified. We have not, however, sampled the bottom of the very deepest bedrock trough, and the pressure regime along its main axis remains unknown.

Another concern is whether our measurements are biased by the melt conditions unique to the 2010–2015 seasons. In particular, the 2010 and 2012 melt seasons were both record warm years with large surface melt production [*Nghiem et al.*, 2012; *van As et al.*, 2012; *Tedesco et al.*, 2013]. Nevertheless, our results include three melt seasons with conditions more similar to the 20 year mean surface mass balance measurements of the K-transect, which passes near our transect of boreholes and likely reflects similar conditions [*van de Wal et al.*, 2012]. Further, our pressure records (including four boreholes with measurements spanning consecutive melt seasons during 2011–2012 and 2012–2013) show no systematic difference between water pressures measured in the high melt years and the average melt years (Figure 8). Although our measurements are influenced by conditions unique to each season, the 5 year total span of the data set is likely broadly representative of multiyear conditions.

Measurements of borehole water pressure at other locations across western GrIS also show similar results to those presented here (Table 2). *Van de Wal et al.* [2015] report melt season water pressure from two boreholes (spaced 5 m apart) located approximately 15 km inland and 2 km south of our transect, ranging approximately 0.93–1.0 OB. *Andrews et al.* [2014] and *Ryser et al.* [2014a, 2014b] report pressure for two melt seasons and two winters (2011–2012) from six boreholes located 20–30 km inland and 250 km northwest of our transect (~600–700 m depth). These records range approximately 0.90–1.13 OB, showing similar seasonal phases and similar differences in magnitude and variability of pressure between closely spaced boreholes (30–40 m). *Lüthi et al.* [2002] measured water pressure for 2 months in two deep boreholes (830 m) spaced ~20 m apart, with weak diurnal cycles and pressure remaining steady near 1.0 OB. Earlier measurements [*Thomsen and Oleson*, 1990, 1991; *Thomsen et al.*, 1991; *Iken et al.*, 1993], although only hours to days in duration, also agree with the observations reported here.

An important exception to the consistency of water pressures is the record from our near-margin borehole M1-10. These data clearly represent a separate hydraulic regime that is an outlier in our data set (Figures 8 and 9) and the observations of other workers. This borehole is likely not representative of overall ablation zone conditions as a result of the site location and shallow ice depth. The site is located only 450 m from the lateral ice sheet margin where subglacial conditions are likely well channelized and tunnels emerge at atmospheric pressure. The relatively thin ice (<100 m) limits creep closure rates, allowing increased conduit cross-sectional area and lower diurnal water pressures [*Röthlisberger*, 1972]. The large diurnal range in pressure at this site is similar to water pressure measured in mountain glacier settings [e.g., *Fudge et al.*, 2008].

To summarize, the consistency we find between multiple topographic regimes and years of measurement, as well as with all previous borehole pressure measurements for the GrIS, implies that our limited point measurements are likely broadly representative of regional conditions. With exception to our shallowest

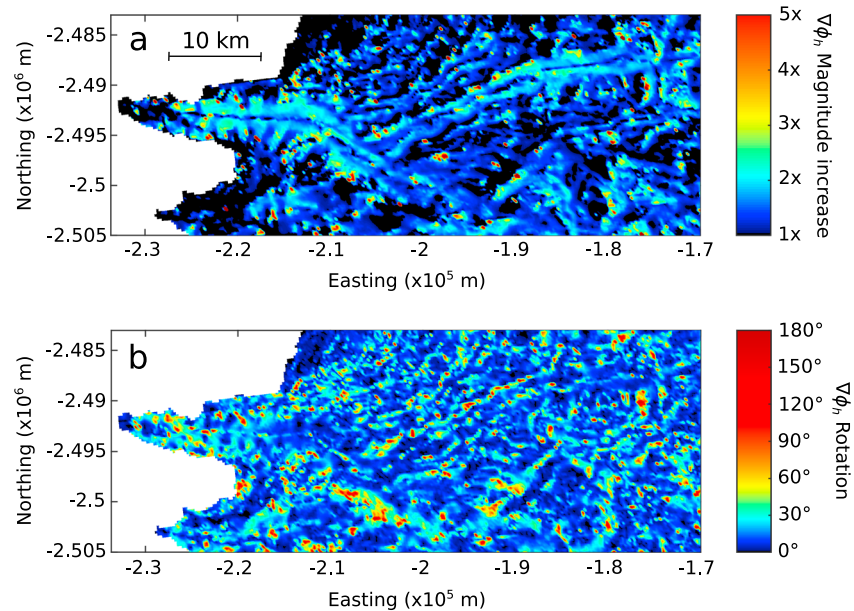


Figure 10. Calculated change in (a) magnitude and (b) rotation of hydraulic potential gradient vectors over a diurnal cycle, using the imposed range of basal water pressure shown by the shaded region in Figure 9 (0.87 OB to 0.99 OB). Black areas in Figure 10a indicate a decrease in gradient magnitude (factor $<1\times$).

near-margin borehole, water pressures throughout the transect are confined within a distinct range of relatively high pressures (approximately 0.8–1.1 OB) and show consistent seasonal phases and a period of regular diurnal cycles. However, our results also show that within the limits of confinement, substantial local variability can be present that may not necessarily be individually upscaled to represent regional conditions.

5.2. Implications for Hydraulic Potential Gradient

5.2.1. Temporal Variability

Our data identify winter water pressures that are relatively steady, suggesting that the limited basal flow during this period is probably constrained by a relatively constant $\nabla\phi_h$ field. Particularly relevant is that the summer pressure field averaged over the daily melt cycle also shows only minor difference from winter pressures (Figure 8). Hence, over a long time average, the hydraulic potential gradient is essentially static. At shorter diurnal time scales, however, observed fluctuations in pressure have the capacity to induce substantial variations in the potential gradient field. This follows from the fact that pressures across the transect reside near overburden levels, so even small fluctuations influence the relative importance of bedrock and surface topography on the $\nabla\phi_h$ field (Figure 1).

To illustrate a plausible impact on $\nabla\phi_h$ due to diurnal swings in the basal pressure field, we consider a semi-empirical conceptual model assuming potential gradients determined solely by the ice overburden as in equation (4). We use surface and bed topography to perform two separate calculations of $\nabla\phi_h$ following equation (4) for imposed values of daily minimum and maximum water pressure that are guided by our observations (see supporting information for details). Comparison of the two $\nabla\phi_h$ fields shows that large changes in both vector magnitude and direction are possible in response to only modest pressure variations (Figure 10). In response to a pressure decline from 0.99 to 0.87 OB, vector magnitude increases over three quarters of the study area, with $\sim 10\%$ of the area demonstrating changes of twofold to threefold (Figure 10). Effects are greatest where bed slopes are steepest and corresponding surface slopes are nearly flat. Vector rotation over the diurnal cycle is controlled by the disparity between surface and bed slope aspects. This is commonly associated with the walls of deep bedrock troughs, which generally have an aspect that is normal to surface slope aspect. This analysis thus demonstrates that despite the relatively static $\nabla\phi_h$ when averaged over long time scales, basal water flow could be highly dynamic in response to the pressure changes that occur over shorter time scales during the melt season.

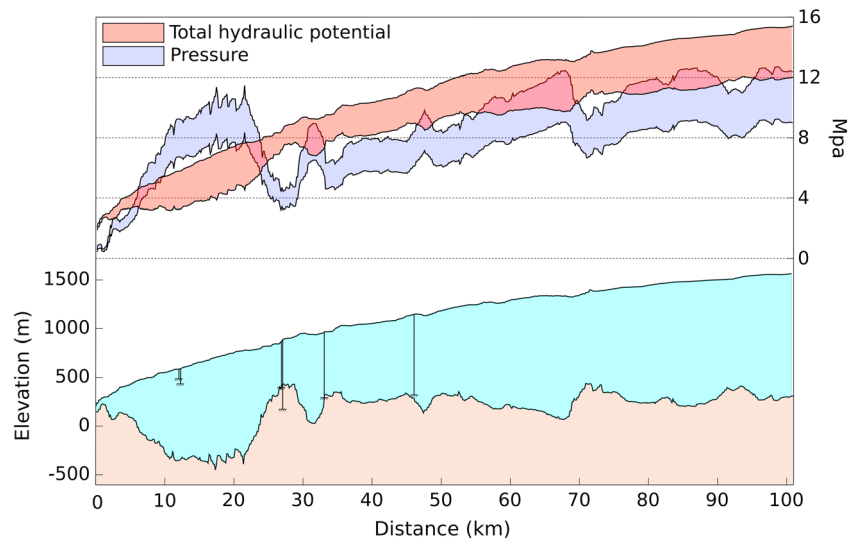


Figure 11. Basal water pressure and total hydraulic potential along the transect line shown in Figure 2 extending to 100 km inland. Ice surface and bed topography along the profile are shown for context, and borehole locations and depths have been projected into the plane of the profile. The shaded bands for both pressure and total hydraulic potential define along-glacier gradients (diminishing from right to left) where the range in values are derived from measured borehole water pressures, ranging 0.8–1.1 of OB. The shaded bands reflect changes in ice thickness and bed elevation combined with variable water pressure stemming from basal processes.

5.2.2. Spatial Variability

Gradients in the hydraulic potential can arise from water pressure changes due to ice thickness variability and from water pressure changes stemming from basal drainage system processes (equation (3)). Our data reveal that both of the water pressure terms in equation (3) make important contributions to the overall hydraulic potential and gradients therein. Yet, while basal processes modify the local overburden pressure, we also find that such modifications are not unlimited but fall within a restricted range. With the exception of locations very close to the margin, all time/space variability occurs within a fixed range of ~ 0.8 to 1.1 OB. As a result, at increasing spatial scales across the ice sheet, hydraulic potential change from ice thickness variation becomes larger than that from water pressure adjustments associated with basal processes. Hence, our transect of basal water pressure measurements implies that the far-field $\nabla\phi_h$ mimics changes in ice thickness but has superimposed local gradients from basal processes (Figure 11). This suggests that the validity of equation (4) is strongly dependent on the spatial scale and the processes of interest.

Water pressure gradients within the drainage system are determined by the distance along flow pathways rather than straight line connections between two geographic locations (or DEM cells). The very conceptualization of $\nabla\phi_h$ is therefore complicated by whether water pressure changes are defined in terms of a discretized topographic domain or along continuous elements of the basal drainage system. This is illustrated by the local gradients we calculate, which reach 20 kPa m^{-1} . Because the calculation is made using a straight line assumption with no knowledge of flow path characteristics, our computed gradients should be viewed as a maximum. Robust and precise calculation of $\nabla\phi_h$ with inclusion of drainage system pressure gradients thus awaits a fuller understanding of the geometry and dynamics of the basal flow system.

Prior studies of hydraulic potential gradients in western Greenland [e.g., Lewis and Smith, 2009; Tedstone et al., 2014; Lindbäck et al., 2015; Chu et al., 2016] including our own analysis in section 5.2.1 have neglected drainage system pressure gradients and flow paths; they are based solely on changes in ice thickness across a cellular topographic domain. Our in situ measurements of basal conditions heed caution to this approach. Despite our finding that far-field $\nabla\phi_h$ follows ice thickness changes, the degree to which our measured local basal process-driven pressure gradients facilitate or hinder broader drainage system reorganization remains uncertain. Thus, specific channel systems, drainage basin areas, and processes related to basin piracy [e.g., Lindbäck et al., 2015; Chu et al., 2016] may not necessarily be captured by water pressure that is a spatially invariant fraction of overburden computed on a cellular topographic domain.

6. Conclusions

Thirteen borehole water pressure records collected across a 46 km transect of the western Greenland Ice Sheet show that basal water pressure undergoes characteristic seasonal phases and is confined within a limited range. Water pressures are relatively steady and high during winter, variable and irregular during spring and fall, and have diurnal cycles that can persist for multiple weeks during the peak melt season. Only a single borehole located 450 m from the ice sheet margin with ice depth <100 m shows relatively low water pressure, ranging between 0.3 and 1.05 of overburden (OB) during the melt season. This record likely represents a channelized hydraulic regime with highly variable meltwater flux and limited creep closure near the ice edge. The remaining 12 boreholes show pressures varying within a confined range, with minimum pressure predominantly greater than 0.8 OB and maximum pressure near or just above overburden. Despite diurnal pressure changes during the summer period, melt season median pressure varies by less than 0.02 OB from winter median pressure for four of five boreholes with overwinter records.

The basal water pressure across the high-relief bed of our western Greenland study area experiences gradients stemming from two sources: changes in ice thickness determining the overburden pressure and changes arising from basal processes. Because water pressure varies within a relatively restricted fraction of overburden, the hydraulic potential gradient most closely mimics the ice thickness when considered over larger spatial scales and time steps that average diurnal swings in pressure. However, on subdaily time scales during the melt season, cycling of pressure can lead to substantial changes in the direction and magnitude of the hydraulic potential gradient. Furthermore, over length scales where the ice thickness does not change substantially, the hydraulic potential is strongly influenced by large gradients resulting from basal drainage system processes.

Acknowledgments

This work is funded by SKB, Posiva, NWMO, NAGRA, the U.S. National Science Foundation (PP-ANS grants 0909495/1203451), and NASA (grant NNX11AM12A). The authors thank Editor Bryn Hubbard and reviewers Martin Lüthi and Peter Jansson for comments that greatly improved the manuscript. Many thanks to the graduate and undergraduate students from University of Montana and University of Wyoming who assisted in field work. Data sets are published by the Swedish Nuclear Waste Management Company referenced by the Greenland Analogue Project at the following web address: <http://www.skb.com/publications/>.

References

- Andrews, L. C., G. A. Catania, M. J. Hoffman, J. D. Gulley, M. P. Lüthi, C. Ryser, R. L. Hawley, and T. A. Neumann (2014), Direct observations of evolving subglacial drainage beneath the Greenland Ice Sheet, *Nature*, *514*(7520), 80–83, doi:10.1038/nature13796.
- Bamber, J. L., et al. (2013), A new bed elevation dataset for Greenland, *Cryosphere*, *7*(2), 499–510, doi:10.5194/tc-7-499-2013.
- Catania, G. A., and T. A. Neumann (2010), Persistent englacial drainage features in the Greenland Ice Sheet, *Geophys. Res. Lett.*, *37*, L02501, doi:10.1029/2009GL041108.
- Chandler, D. M., et al. (2013), Evolution of the subglacial drainage system beneath the Greenland Ice Sheet revealed by tracers, *Nat. Geosci.*, *6*(3), 195–198, doi:10.1038/ngeo1737.
- Chu, W., T. T. Creyts, and R. E. Bell (2016), Rerouting of subglacial water flow between neighboring glaciers in west Greenland, *J. Geophys. Res. Earth Surf.*, doi:10.1002/2015JF003705.
- Cuffey, K. M., and W. S. B. Paterson (2010), *The Physics of Glaciers*, 4th ed., Academic Press, London.
- Das, S. B., I. Joughin, M. D. Behn, I. M. Howat, M. A. King, D. Lizarralde, and M. P. Bhatia (2008), Fracture propagation to the base of the Greenland Ice Sheet during supraglacial lake drainage, *Science*, *320*(5877), 778–781, doi:10.1126/science.1153360.
- Fountain, A., and J. Walder (1998), Water flow through temperate glaciers, *Rev. Geophys.*, *36*(3), 299–328, doi:10.1029/97RG03579.
- Fudge, T. J., N. F. Humphrey, J. T. Harper, and W. T. Pfeffer (2008), Diurnal fluctuations in borehole water levels: Configuration of the drainage system beneath Bench Glacier, Alaska, USA, *J. Glaciol.*, *54*(185), 297–306, doi:10.3189/002214308784886072.
- Harrington, J. A., N. F. Humphrey, and J. T. Harper (2015), Temperature distribution and thermal anomalies along a flowline of the Greenland Ice Sheet, *Ann. Glaciol.*, *56*(70), 98–104, doi:10.3189/2015AoG70A945.
- Hewitt, I. J. (2013), Seasonal changes in ice sheet motion due to melt water lubrication, *Earth Planet. Sci. Lett.*, *371*–372, 16–25, doi:10.1016/j.epsl.2013.04.022.
- Hewitt, I. J., C. Schoof, and M. A. Werder (2012), Flotation and free surface flow in a model for subglacial drainage. Part 2. Channel flow, *J. Fluid Mech.*, *702*, 157–187, doi:10.1017/jfm.2012.166.
- Hoffman, M. J., G. A. Catania, T. A. Neumann, L. C. Andrews, and J. A. Rumrill (2011), Links between acceleration, melting, and supraglacial lake drainage of the western Greenland Ice Sheet, *J. Geophys. Res.*, *116*, F04035, doi:10.1029/2010JF001934.
- Hooke, R. L. (1989), Englacial and subglacial hydrology: A qualitative review, *Arct. Alp. Res.*, *21*(3), 221–233, doi:10.2307/1551561.
- Hubbard, B., and P. Nienow (1997), Alpine subglacial hydrology, *Quat. Sci. Rev.*, *16*(9), 939–955, doi:10.1016/S0277-3791(97)00031-0.
- Humphrey, N., and K. Echelmeyer (1990), Hot-water drilling and bore-hole closure in cold ice, *J. Glaciol.*, *36*(124), 287–298, doi:10.3189/002214390793701354.
- Iken, A., K. Echelmeyer, W. Harrison, and M. Funk (1993), Mechanisms of fast flow in Jakobshavn Isbrae, west Greenland: Part I. Measurements of temperature and water level in deep boreholes, *J. Glaciol.*, *39*(131), 15–25.
- Lewis, S. M., and L. C. Smith (2009), Hydrologic drainage of the Greenland Ice Sheet, *Hydrol. Process.*, *23*(14).
- Lindbäck, K., R. Pettersson, S. H. Doyle, C. Helanow, P. Jansson, S. S. Kristensen, L. Stenseng, R. Forsberg, and A. L. Hubbard (2014), High-resolution ice thickness and bed topography of a land-terminating section of the Greenland Ice Sheet, *Earth Syst. Sci. Data*, *6*(2), 331–338, doi:10.5194/essd-6-331-2014.
- Lindbäck, K., R. Pettersson, A. L. Hubbard, S. H. Doyle, D. van As, A. B. Mikkelsen, and A. A. Fitzpatrick (2015), Subglacial water drainage, storage, and piracy beneath the Greenland Ice Sheet, *Geophys. Res. Lett.*, *42*, 7606–7614, doi:10.1002/2015GL065393.
- Liston, G. E., and S. H. Mernild (2012), Greenland freshwater runoff. Part I: A runoff routing model for glaciated and nonglaciated landscapes (HydroFlow), *J. Clim.*, *25*(17), 5997–6014, doi:10.1175/JCLI-D-11-00591.1.
- Livingstone, S. J., C. D. Clark, J. Woodward, and J. Kingslake (2013), Potential subglacial lake locations and meltwater drainage pathways beneath the Antarctic and Greenland Ice Sheets, *Cryosphere*, *7*(6), 1721–1740, doi:10.5194/tc-7-1721-2013.

- Lüthi, M., M. Funk, A. Iken, S. Gogineni, and M. Truffer (2002), Mechanisms of fast flow in Jakobshavn Isbrae, west Greenland: Part III. Measurements of ice deformation, temperature and cross-borehole conductivity in boreholes to the bedrock, *J. Glaciol.*, *48*(162), 369–385, doi:10.3189/172756502781831322.
- McGrath, D., W. Colgan, K. Steffen, P. Lauffenburger, and J. Balog (2011), Assessing the summer water budget of a moulin basin in the Sermeq Avannarleq ablation region, Greenland Ice Sheet, *J. Glaciol.*, *57*(205), 954–964, doi:10.3189/002214311798043735.
- Meierbachtol, T., J. Harper, and N. Humphrey (2013), Basal drainage system response to increasing surface melt on the Greenland Ice Sheet, *Science*, *341*(6147), 777–779, doi:10.1126/science.1235905.
- Morlighem, M., E. Rignot, J. Mouginot, H. Seroussi, and E. Larour (2014), Deeply incised submarine glacial valleys beneath the Greenland Ice Sheet, *Nat. Geosci.*, *7*(6), 18–22, doi:10.1038/ngeo2167.
- Nghiem, S. V., D. K. Hall, T. L. Mote, M. Tedesco, M. R. Albert, K. Keegan, C. A. Shuman, N. E. DiGirolamo, and G. Neumann (2012), The extreme melt across the Greenland Ice Sheet in 2012, *Geophys. Res. Lett.*, *39*, L20502, doi:10.1029/2012GL053611.
- Röthlisberger, H. (1972), Water pressure in intra- and subglacial channels, *J. Glaciol.*, *11*(62).
- Ryser, C., M. P. Lüthi, L. C. Andrews, G. A. Catania, M. Funk, R. Hawley, M. J. Hoffman, and T. A. Neumann (2014a), Caterpillar-like ice motion in the ablation zone of the Greenland Ice Sheet, *J. Geophys. Res. Earth Surf.*, *119*, 2258–2271, doi:10.1002/2013JF003067.
- Ryser, C., M. P. Lüthi, L. C. Andrews, M. J. Hoffman, G. A. Catania, R. L. Hawley, T. A. Neumann, and S. S. Kristensen (2014b), Sustained high basal motion of the Greenland Ice Sheet revealed by borehole deformation, *J. Glaciol.*, *60*(222), 647–660, doi:10.3189/2014JoG13J196.
- Shreve, R. L. (1972), Movement of water in glaciers, *J. Glaciol.*, *11*(62), 205–214.
- Tedesco, M., X. Fettweis, T. Mote, J. Wahr, P. Alexander, J. E. Box, and B. Wouters (2013), Evidence and analysis of 2012 Greenland records from spaceborne observations, a regional climate model and reanalysis data, *Cryosphere*, *7*(2), 615–630, doi:10.5194/tc-7-615-2013.
- Tedstone, A. J., P. W. Nienow, N. Gourmelen, and A. J. Sole (2014), Greenland Ice Sheet annual motion insensitive to spatial variations in subglacial hydraulic structure, *Geophys. Res. Lett.*, *41*, 8910–8917, doi:10.1002/2014GL062386.
- Thomsen, H. H., and O. B. Olesen (1990), Continued glaciological investigations with respect to hydropower and ice-climate relationships at Pakitsoq, Jakobshavn, west Greenland, *Rapp. Gronl. Geol. Unders.*, *148*, 83–86.
- Thomsen, H. H., and O. B. Olesen (1991), Hydraulics and hydrology on the Inland Ice, *Rapp. Gronl. Geol. Unders.*, *152*, 36–38.
- Thomsen, H. H., O. B. Olesen, R. J. Braithwaite, and C. E. Boggild (1991), Ice drilling and mass balance at Pakitsoq, Jakobshavn, central west Greenland, *Rapp. Gronl. Geol. Unders.*, *152*, 80–84.
- van As, D., A. L. Hubbard, B. Hasholt, A. B. Mikkelsen, M. R. van den Broeke, and R. S. Fausto (2012), Large surface meltwater discharge from the Kangerlussuaq sector of the Greenland Ice Sheet during the record-warm year 2010 explained by detailed energy balance observations, *Cryosphere*, *6*(1), 199–209, doi:10.5194/tc-6-199-2012.
- van de Wal, R. S. W., W. Boot, C. J. P. P. Smeets, H. Snellen, M. R. van den Broeke, and J. Oerlemans (2012), Twenty-one years of mass balance observations along the K-transect, west Greenland, *Earth Syst. Sci. Data*, *4*(1), 31–35, doi:10.5194/essd-4-31-2012.
- van de Wal, R. S. W., et al. (2015), Self-regulation of ice flow varies across the ablation area in south-west Greenland, *Cryosphere*, *9*(2), 603–611, doi:10.5194/tc-9-603-2015.
- Werder, M. A., I. J. Hewitt, C. G. Schoof, and G. E. Flowers (2013), Modeling channelized and distributed subglacial drainage in two dimensions, *J. Geophys. Res. Earth Surf.*, *118*, 2140–2158, doi:10.1002/jgrf.20146.